

Displacement-Squeeze receiver for BPSK displaced squeezed vacuum states surpassing the coherent-states Helstrom bound under imperfect conditions

Enhao Bai

*Information Support Force Engineering University, Wuhan 430035, China and
Guangxi Key Laboratory of Multimedia Communications and Network Technology, Guangxi University, Nanning 530006, China*

Jian Peng, Tianyi Wu, and Chen Dong^{*}

Information Support Force Engineering University, Wuhan 430035, China

Kai Wen, Fengkai Sun, and Zhenrong Zhang[†]

Guangxi Key Laboratory of Multimedia Communications and Network Technology, Guangxi University, Nanning 530006, China

Chun Zhou

Henan Key Laboratory of Quantum Information and Cryptography, SSF IEU, Zhengzhou 450001, China

Yaping Li

Wuhan Maritime Communication Research Institute, Wuhan 430035, China

(Dated: January 15, 2026)

We propose a displacement-squeeze receiver (DSR) for discriminating BPSK displaced squeezed vacuum states (S-BPSK). The receiver applies a displacement followed by a squeezing operation with the squeezing axis rotated by $\frac{\pi}{2}$, and performs photon-number-resolving detection with a MAP threshold decision. This processing effectively increases the distinguishability of the input states by elongating their distance in phase space and reducing their population overlap in Fock basis. We show that for all signal energy N , $P_{\text{err}}^{\text{DSR}} \in [P_{\text{HB}}^{\text{DSS}}, 2P_{\text{HB}}^{\text{DSS}}]$, under equal priors and ideal condition. In the low-energy regime, DSR beats the S-BPSK SQL at $N \approx 0.3$ and drops below the coherent-state BPSK (C-BPSK) Helstrom bound at $N \approx 0.4$, reaching $P_{\text{err}}^{\text{DSR}} < 1\%$ near $N \approx 0.6$. Finally, we quantify performance under non-unit efficiency and dark counts, phase diffusion, and receiver thermal noise, with MAP threshold adaptation providing robustness across these nonidealities.

I. INTRODUCTION

As an important topic in the field of quantum information, quantum-states discrimination directly affects the performance of quantum communication systems. To date, we have consistently regarded coherent states (CSs) as carriers for quantum communication and have proposed numerous excellent discrimination schemes, such as the Kennedy receiver[1], the optimized displacement receiver[2], multi-stage receiver[3–6], the conditional pulse nulling receiver[7], and hybrid receiver [8–11]. This is primarily because coherent states retain their coherence after passing through lossy bosonic channels, demonstrating that they can maintain state purity in most optical transmission media, including but not limited to free space and optical fibers.[12–14]. However, coherent states have inherent discrimination limitations: any two coherent states are non-orthogonal and exhibit overlap in phase space. Since the Helstrom Bound (HB) is closely related to the degree of overlap between quantum states[15, 16], coherent states have a theoretical lower bound on discrimination error probability.

In recent years, quantum-state discrimination schemes based on non-Poissonian photon statistics have attracted widespread attention[17–22]. For example, Giovanni Chesi and Stefano Olivares proposed using squeezed vacuum states ($\hat{S}(r)|0\rangle$ where $\hat{S}(r), r \in \mathbf{R}_+$ is squeeze operator and $|0\rangle$ is vacuum state) as information carriers to construct a binary communication channel[20]. By applying a displacement operation $\hat{D}(\pm\alpha)$ to the squeezed vacuum state, two phase-opposite displaced squeezed vacuum states (DSSs) $|\pm\alpha, r\rangle$ can be generated. Then they encoded BPSK symbols into two phase-opposite DSSs (S-BPSK):

$$\begin{cases} \text{symbol '0'} : |\psi_0\rangle = \hat{D}(-\alpha)\hat{S}(r)|0\rangle = |-\alpha, r\rangle \\ \text{symbol '1'} : |\psi_1\rangle = \hat{D}(+\alpha)\hat{S}(r)|0\rangle = |+\alpha, r\rangle \end{cases} \quad (1)$$

^{*} dongchengfkd@163.com

[†] zrz76@gxu.edu.cn

This scheme significantly reduces the overlap between the carrier states by squeezing its position quadrature \hat{X} . Theoretical studies show that when the communication channel energy N is fixed, not only the HB for S-BPSK can be significantly lower than that for BPSK coherent states (C-BPSK), but the error probability of homodyne detection (Standard Quantum Limit, SQL) for S-BPSK can even surpass the HB for C-BPSK at a low mean photon number of $N \approx 0.659$ [20].

Unlike the work of Giovanni Chesi and Stefano Olivares, this paper proposes a quantum-enhanced receiver for discriminating the S-BPSK signal, which is called as the Displacement-Squeeze Receiver (DSR). The DSR combines Gaussian operations (displacement and squeeze) and photon-number-resolving detection to approach the Helstrom bound for S-BPSK within a constant factor, while outperforming coherent-state receivers in the low-energy regime. Theoretical analysis shows that, for the same input mean photon number, the DSR can achieve an error probability lower than the Helstrom bound for C-BPSK channels in the low-photon-number regime. For example, when $N \approx 0.6$ the error probability falls below 1% in our simulations.

The structure of this paper is as follows: Section II reviews the fundamental theory of S-BPSK discrimination; Section III provides a detailed analysis of the principle and performance of the DSR; Section IV explores the performance of DSR under non-ideal conditions, including non-ideal PNR detectors (quantum efficiency η and dark count rate ν), phase diffusion noise in the channel, and receiver thermal noise; finally, the paper is summarized, and potential application scenarios are discussed.

II. CHANNEL MODEL AND PERFORMANCE BENCHMARKS

In this section we summarize the signal model and the fundamental performance limits for binary phase-shift keyed (BPSK) communication based on displaced squeezed vacuum states, and we fix the notation used in the rest of the paper.

For binary discrimination between quantum states $|\psi_0\rangle$ and $|\psi_1\rangle$ with prior probabilities $P_0 = P_1 = \frac{1}{2}$, the minimum error probability (Helstrom bound) is given by [15, 20]:

$$\begin{aligned} P_{\text{HB}}^{\text{DSS}}(\alpha, r) &= \frac{1}{2} \left(1 - \sqrt{1 - |\langle \psi_0 | \psi_1 \rangle|^2} \right) \\ &= \frac{1}{2} \left(1 - \sqrt{1 - \exp(-4\alpha^2 e^{2r})} \right) \end{aligned} \quad (2)$$

As a practically relevant benchmark we also consider homodyne detection along the X quadrature, which attains the standard quantum limit (SQL) for BPSK under ideal conditions. Given the input is $\rho_i = |\psi_i\rangle \langle \psi_i|$, the conditional probability density of the homodyne outcome x ,

$$\begin{aligned} P(x|\rho_i) &= \int_{-\infty}^{+\infty} dp \cdot W(x, p|\rho_i) \\ &= \frac{e^r}{\sqrt{\pi}} \exp \left\{ -e^{2r} \left[x - (-1)^{i+1} \sqrt{2} \alpha \right]^2 \right\}, \quad i \in 0, 1, \end{aligned} \quad (3)$$

which $W(x, p|\rho_i)$ is the Wigner function of ρ_i (see Appendix). And the resulting error probability is

$$P_{\text{SQL}}^{\text{DSS}} = \int_0^{+\infty} P(x|\rho_0) dx = \frac{1}{2} \text{erfc} \left(\sqrt{2} \alpha e^r \right) \quad (4)$$

To parameterize the contribution of squeezing, we introduce the squeezing fraction

$$\beta := \frac{\sinh^2(r)}{N} \quad (5)$$

which quantifies the share of the total energy ($N = |\alpha|^2 + \sinh^2(r)$) stored in squeezing [20]. Therefore, the parameter α and r can be expressed as

$$\begin{cases} \alpha = \sqrt{N(1-\beta)}, & r = \sinh^{-1} \sqrt{N\beta} \\ \alpha e^r = \sqrt{N(1-\beta)} \left(\sqrt{1+N\beta} + \sqrt{N\beta} \right) \end{cases} \quad (6)$$

Accordingly, both the Helstrom bound and the SQL for S-BPSK become functions of (N, β) , denoted $P_{\text{SQL}}^{\text{DSS}}(N, \beta)$, and $P_{\text{HB}}^{\text{DSS}}(N, \beta)$. The squeezing fraction can be optimized at fixed total energy. By minimizing $P_{\text{HB}}^{\text{DSS}}(N, \beta)$ over β one obtains the optimal value [20]:

$$\beta_{\text{opt}}(N) = \frac{N}{2N + 1} \quad (7)$$

Therefore, $\alpha^2 e^{2r} = N(N + 1)$. Both the Helstrom bound and the SQL for S-BPSK are rewritten as:

$$P_{\text{SQL}}^{\text{DSS}}(N, \beta_{\text{opt}}) = \frac{1}{2} \text{erfc} \left(\sqrt{2N(N + 1)} \right) \quad (8)$$

$$P_{\text{HB}}^{\text{DSS}}(N, \beta_{\text{opt}}) = \frac{1}{2} \left(1 - \sqrt{1 - \exp \{-4N(N + 1)\}} \right) \quad (9)$$

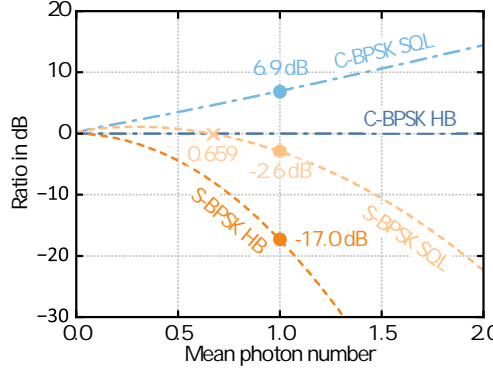


FIG. 1. The ratios of $P_{\text{HB}}^{\text{DSS}}(N, \beta_{\text{opt}})$, $P_{\text{SQL}}^{\text{DSS}}(N, \beta_{\text{opt}})$ and $P_{\text{SQL}}^{\text{CS}}(N)$ to $P_{\text{HB}}^{\text{CS}}(N)$ vs. input state energy N . Here, $P_{\text{SQL}}^{\text{CS}}(N) = \frac{1}{2} \left[1 - \text{erf} \left(\sqrt{2 \cdot N} \right) \right]$ and $P_{\text{HB}}^{\text{CS}}(N) = \frac{1}{2} \left[1 - \sqrt{1 - \exp \{-4 \cdot N\}} \right]$.

When the DSSs are prepared with this choice, the S-BPSK Helstrom bound is significantly lower than that of C-BPSK at the same energy. In particular, for $N \approx 1$ the S-BPSK Helstrom bound already reaches the order of 10^{-4} , whereas C-BPSK requires approximately twice the energy to achieve a comparable error probability. Moreover, in the low-photon number regime the S-BPSK SQL can fall below the Helstrom bound of C-BPSK, with the crossover occurring around $N \approx 0.659$ (see Fig. 1). At $N = 1.0$, the HB for S-BPSK surpasses the SQL for C-BPSK by a remarkable 17.39dB, and the SQL for S-BPSK also is 2.94dB lower. In the subsequent analyses, all DSSs employ the optimal squeezing fraction β_{opt} .

III. QUANTUM-ENHANCED RECEIVER FOR DISCRIMINATING BPSK DISPLACED SQUEEZED VACUUM STATES

We propose a quantum-enhanced receiver for S-BPSK discrimination, referred to as the displacement-squeeze receiver (DSR). Its schematic is shown in Fig. 2. Compared with conventional displacement receivers, the DSR introduces an additional squeezing operation. The squeezing strength matches that used at the transmitter, whereas the squeezing axis is rotated by $\pi/2$ in phase space.

In the DSR, the input state $\rho_i = |\psi_i\rangle\langle\psi_i|$ first interferes with a local oscillator $|\alpha\rangle$ on a highly transmissive beam splitter ($\tau \rightarrow 1$), implementing the displacement operation $D(\alpha)$. This maps the BPSK pair $\{|\alpha, r\rangle, |\alpha, -r\rangle\}$ to an OOK-like pair $\{|0, r\rangle, |+2\alpha, r\rangle\}$. Subsequently, a squeezing operation $S(-r)$ is applied, squeezing the P quadrature. The processed state is denoted by

$$\zeta_i = U \rho_i U^\dagger, \quad U = S(-r) D(\alpha). \quad (10)$$

A PNR detector then measures ζ_i and outputs the photon number n , based on which the receiver makes a MAP decision.

We next provide an intuitive explanation of the DSR advantage. Figs. 3(a)–(c) illustrate how the phase-space distributions evolve under the displacement and squeezing operations for $N = 1.0$ and $\beta = \beta_{\text{opt}}$. The two input

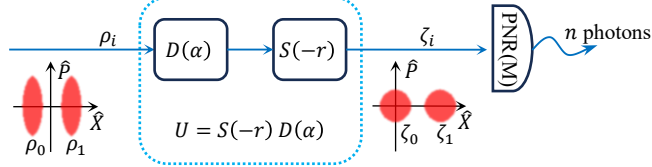


FIG. 2. Schematic of the proposed DSR. The input state ρ_i is transformed to ζ_i via a displacement followed by a squeezing operation, $U = S(-r)D(\alpha)$, and is then measured by a photon-number-resolving (PNR) detector with outcome n . The final decision is made according to the maximum a posteriori (MAP) criterion.

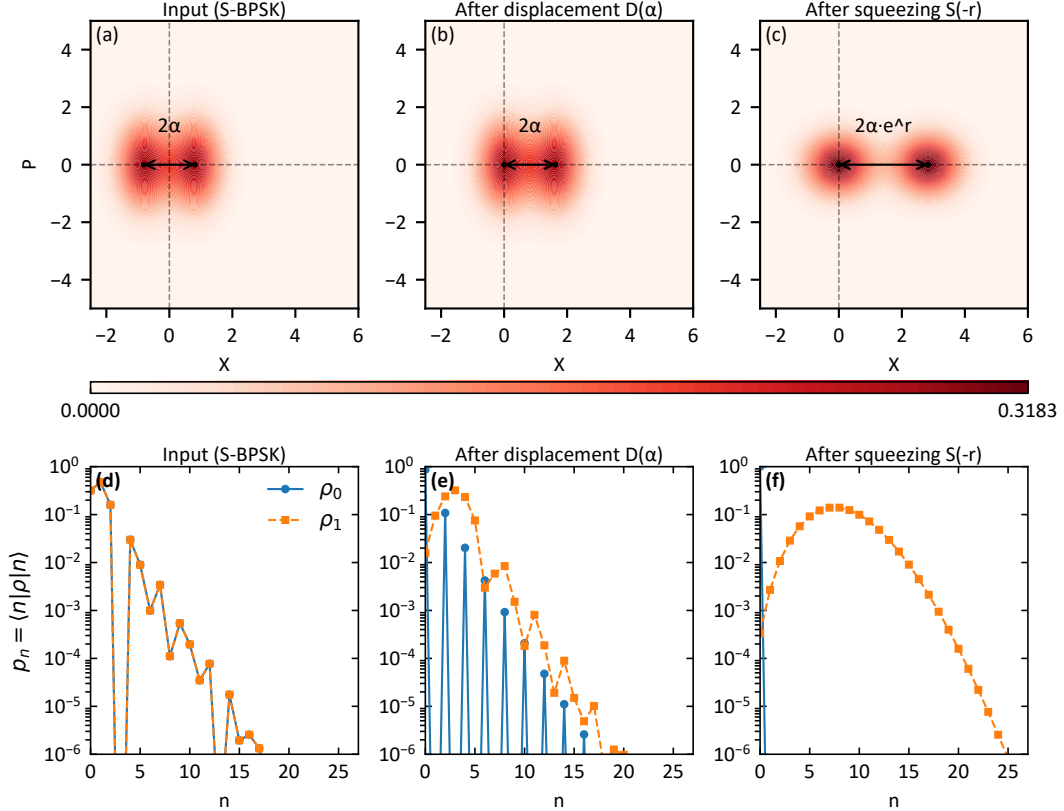


FIG. 3. Phase-space representations (a–c) and Fock-basis populations (d–f) of the input states ρ_i in the DSR for mean photon number $N = 1.0$ and squeezing fraction $\beta = \beta_{\text{opt}}$. Panels (a) and (d) show the input states ρ_i ; panels (b) and (e) show the states after the displacement operation $D\rho_i D^\dagger$; and panels (c) and (f) show the states after the full DSR transformation $\zeta_i = U\rho_i U^\dagger$.

states ρ_0 and ρ_1 are separated by $\Delta = 2\alpha$ in phase space. After the displacement operation, the two states become a squeezed vacuum state and a displaced squeezed vacuum state (Fig. 3(b)):

$$\begin{cases} D(\alpha) \cdot |\psi_0\rangle = S(r) |0\rangle \\ D(\alpha) \cdot |\psi_1\rangle = D(2\alpha) S(r) |0\rangle \end{cases} \quad (11)$$

The displacement does not change the separation $\Delta = 2\alpha$ between the state centroids in phase space; however, it leads to distinct Fock-basis populations for ρ_0 and ρ_1 (see Figs. 3(d) and (e)).

After the subsequent squeezing operation, the two states evolve into the vacuum state and a coherent state, respectively (Fig. 3(c)):

$$\begin{cases} U \cdot |\psi_0\rangle = |0\rangle \\ U \cdot |\psi_1\rangle = S(-r) D(2\alpha) S(r) |0\rangle = D(\gamma) |0\rangle = |\gamma\rangle \end{cases} \quad (12)$$

Here,

$$\begin{aligned}\gamma &= 2\alpha \cdot \cosh(r) + 2\alpha^* \cdot \sinh(r) \\ &= 2\alpha \cdot e^r > 2\alpha,\end{aligned}\tag{13}$$

where the last equality assumes α is real (i.e., the phase reference is chosen such that $\alpha \in \mathbb{R}$). Therefore, the S-BPSK input $\rho_i \in \{|-\alpha, r\rangle, |\alpha, r\rangle\}$ is converted into a coherent-state OOK pair $\zeta_i \in \{|0\rangle, |\gamma\rangle\}$. Importantly, the phase-space separation increases from 2α to $\gamma = 2\alpha e^r$, enhancing distinguishability for subsequent PNR detection. By comparison, a coherent-state displacement receiver (without squeezing) yields a separation $\Delta_C = 2\sqrt{N}$, whereas the DSR produces $\gamma = 2\sqrt{N(N+1)}$.

Figs. 3(d)–(f) show the corresponding changes in Fock-basis populations. After the squeezing operation (Fig. 3(f)), the population associated with ρ_1 shifts toward higher photon numbers, while the population associated with ρ_0 concentrates near $n = 0$. Consequently, the overlap between the two photon-number distributions is reduced, facilitating discrimination with a PNR detector.

A. PNR detection model and MAP decision rule

We now incorporate finite PNR resolution. A PNR detector with resolution M is denoted as $\text{PNR}(M)$ and is described by the POVM elements

$$\begin{aligned}\Pi_n &= |n\rangle \langle n|, \quad n = 0, 1, \dots, M-1 \\ \Pi_M &= \mathbf{I} - \sum_{i=0}^{M-1} \Pi_i\end{aligned}\tag{14}$$

where \mathbf{I} is the identity operator in the Fock basis. For a measured coherent state ρ with mean photon number μ , the conditional probability of obtaining outcome n is

$$q_n^M(\mu) = \text{Tr}\{\Pi_n \cdot \rho\} = \begin{cases} e^{-\mu} \cdot \frac{\mu^n}{n!}, & n \leq M-1 \\ 1 - e^{-\mu} \cdot \sum_{j=0}^{M-1} \frac{\mu^j}{j!}, & n = M \end{cases}\tag{15}$$

Accordingly, the conditional probability of outcome n given that symbol i was sent is

$$P(n|i) = \text{Tr}(\Pi_n \cdot \zeta_i) = \begin{cases} q_n^M(0), & i = 0 \\ q_n^M(|\gamma|^2), & i = 1 \end{cases}\tag{16}$$

The MAP decision rule for binary discrimination can be equivalently expressed as an optimal threshold test on n [23, 24], summarized in Table I. The corresponding threshold n_{th}^* satisfies Eq. (17).

$$\begin{aligned}P_0 \cdot P(n|0) &\geq P_1 \cdot P(n|1), \text{ where } n \leq n_{\text{th}}^* \\ \Rightarrow n_{\text{th}}^* &= \min\{\lceil n \rceil, M\}\end{aligned}\tag{17}$$

where, $\lceil \cdot \rceil$ denotes the ceiling function (rounding up); Under ideal and equal-prior probability conditions, one obtains $n_{\text{th}}^* = 1$.

TABLE I. Threshold decision strategy of the DSR. If the $\text{PNR}(M)$ outcome satisfies $n < n_{\text{th}}^*$, decide symbol ‘0’; otherwise decide symbol ‘1’.

The outcomes of $\text{PNR}(M)$	Decision
$n \geq n_{\text{th}}^*$	symbol ‘1’
$n < n_{\text{th}}^*$	symbol ‘0’

B. Error probability under ideal conditions

Now we analyze the error probability of the DSR. Assuming the optimal threshold value is n_{th}^* , the threshold decision strategy (see Table. I) can be expressed using POVM operators:

$$\begin{aligned} \text{symbol '0'} : \quad \Pi_{\text{off}} &= \sum_{n=0}^{n_{th}^*-1} \Pi_n = \sum_{n=0}^{n_{th}^*-1} |n\rangle \langle n| \\ \text{symbol '1'} : \quad \Pi_{\text{on}} &= \mathbf{I} - \Pi_{\text{off}} \end{aligned} \quad (18)$$

The average error probability is then

$$\begin{aligned} P_{\text{err}}^{\text{DSR}} &= 1 - \frac{1}{2} [P(C|0) + P(C|1)] \\ &= 1 - \frac{1}{2} [\mathbf{Tr}(\Pi_{\text{off}} \cdot \zeta_0) + \mathbf{Tr}(\Pi_{\text{on}} \cdot \zeta_1)] \end{aligned} \quad (19)$$

where $P(C|i)$ denotes the probability of a correct decision conditioned on sending symbol i . Under ideal conditions, $n_{th}^* = 1$, hence $\Pi_{\text{off}} = |0\rangle \langle 0|$, $\Pi_{\text{on}} = \mathbf{I} - |0\rangle \langle 0|$. The DSR error probability becomes

$$\begin{aligned} P_{\text{err}}^{\text{DSR}} &= 1 - \frac{1}{2} [q_0^M(0) + 1 - q_0^M(|\gamma|^2)] \\ &= \frac{1}{2} \exp\{-4|\alpha|^2 e^{2r}\} = \frac{1}{2} \exp\{-4N(N+1)\} \end{aligned} \quad (20)$$

Eq. (20) shows that, under ideal conditions, $P_{\text{err}}^{\text{DSR}}$ is independent of the PNR resolution M . Therefore, in the numerical results of Fig. 4, we consider PNR(1), i.e., a single-photon detector (SPD).

For S-BPSK, the Helstrom bound in Eq. (9) and the DSR error probability in Eq. (20) satisfy

$$\frac{P_{\text{err}}^{\text{DSR}}}{P_{\text{HB}}^{\text{DSS}}} = \frac{\exp\{-4N(N+1)\}}{1 - \sqrt{1 - \exp\{-4N(N+1)\}}} \quad (21)$$

In the low-energy limit $N \rightarrow 0$, both $P_{\text{err}}^{\text{DSR}}$ and $P_{\text{HB}}^{\text{DSS}}$ approach 0.5 and the ratio tends to 1, corresponding to random guessing. In the high-energy regime $N \gg 1$, the ratio approaches 2 (i.e., 3 dB), yielding

$$P_{\text{err}}^{\text{DSR}} \simeq 2P_{\text{HB}}^{\text{DSS}} \quad (22)$$

Although the DSR remains suboptimal with respect to the Helstrom bound of S-BPSK and satisfies $P_{\text{err}}^{\text{DSR}} \in [P_{\text{HB}}^{\text{DSS}}, 2P_{\text{HB}}^{\text{DSS}}]$ for all N , it still provides a substantial advantage over C-BPSK channels. In particular, for the same mean photon number N , the proposed DSR can achieve an error probability below the Helstrom bound $P_{\text{HB}}^{\text{CS}}$ of a C-BPSK channel; for example, around $N \approx 0.4$ in Fig. 4 the DSR performance lies between the DSS Helstrom bound and the coherent state Helstrom bound.

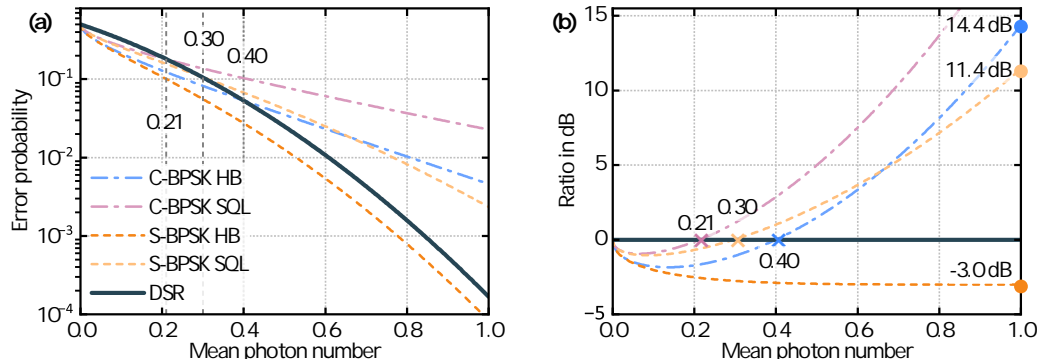


FIG. 4. Performance of the DSR with an SPD under ideal conditions. (a) Error probability of the DSR. (b) Ratio (in dB) of the benchmarks $P_{\text{HB}}^{\text{CS}}$, $P_{\text{SQL}}^{\text{CS}}$, $P_{\text{HB}}^{\text{DSS}}$, and $P_{\text{SQL}}^{\text{DSS}}$ relative to $P_{\text{err}}^{\text{DSR}}$.

Figure 4(a) shows the DSR error probability as a function of the mean photon number. The DSR surpasses the C-BPSK SQL, the S-BPSK SQL, and the C-BPSK Helstrom bound at $N \approx 0.21, 0.30$, and 0.40 , respectively. As N increases, the performance advantage over these benchmarks grows. At $N = 1.0$, the DSR achieves gains of 21.3 dB, 11.4 dB, and 14.4 dB relative to the C-BPSK SQL, the S-BPSK SQL, and the C-BPSK Helstrom bound, respectively, while remaining 3 dB above the S-BPSK Helstrom bound, as summarized in Fig. 4(b). These results demonstrate that the DSR provides strong performance over a broad photon-number regime.

The above analysis assumes ideal, noiseless conditions. In the next section, we examine the impact of non-ideal factors on receiver performance, including imperfect photon detection, phase diffusion, and thermal noise.

IV. THE PERFORMANCE OF DSR UNDER REALISTIC CONDITIONS

A. The quantum efficiency η and the dark count rate ν of PNR(M)

The realistic factors of PNR detectors include quantum efficiency η and dark count rate ν . Quantum efficiency essentially corresponds to photon loss during detection, while dark count rate fundamentally arises from random triggering events caused by environmental noise [25, 26]. Under ideal conditions, quantum efficiency $\eta = 1$ and dark count rate $\nu = 0$. If we simultaneously consider imperfect quantum efficiency $\eta < 1$ and dark count rate $\nu > 0$, the POVM operators for PNR(M) (Eq. (14)) are rewritten as [27]:

$$\Pi_n = e^{-\nu} \sum_{l=0}^n \sum_{k=n-l}^{\infty} \frac{\nu^l}{l!} C_{n-l}^k \cdot \eta^{n-l} (1-\eta)^{k-(n-l)} |k\rangle \langle k|, \quad n = 0, \dots, M \quad (23)$$

At this point, the probability of PNR(M) detecting n photons (Eq. (15)) is rewritten as:

$$q_n^M(\mu, \eta, \nu) = \begin{cases} e^{-(\eta\mu+\nu)} \cdot \frac{(\eta\mu+\nu)^n}{n!}, & n \leq M-1 \\ 1 - e^{-(\eta\mu+\nu)} \cdot \sum_{j=0}^{M-1} \frac{(\eta\mu+\nu)^j}{j!}, & n = M \end{cases} \quad (24)$$

By substituting into Eq. (17), the optimal threshold n_{th}^* is obtained:

$$n_{th}^* = \min \left\{ \left\lceil \frac{\eta|\gamma|^2}{\ln(\eta|\gamma|^2 + \nu) - \ln \nu} \right\rceil, M \right\} = \min \left\{ \left\lceil \frac{\eta \cdot 4N(N+1)}{\ln(\eta \cdot 4N(N+1) + \nu) - \ln \nu} \right\rceil, M \right\} \quad (25)$$

If only consider quantum efficiency ($\eta < 1, \nu = 0$), the optimal threshold n_{th}^* remains 1 ($\frac{\eta|\gamma|^2}{\ln(\eta|\gamma|^2 + \nu) - \ln \nu} \rightarrow 0^+$, $\left\lceil \frac{\eta|\gamma|^2}{\ln(\eta|\gamma|^2 + \nu) - \ln \nu} \right\rceil \rightarrow 1$). Then, the error probability expression (Eq. (20)) is rewritten as:

$$\begin{aligned} P_{\text{err}}^{\text{DSR}}(N, \eta) &= 1 - \frac{1}{2} [q_0^M(0, \eta) + 1 - q_0^M(|\gamma|^2, \eta)] \\ &= \frac{1}{2} \exp \{-4|\alpha|^2 \cdot e^{2r} \cdot \eta\} = \frac{1}{2} \exp \{-4N(N+1) \cdot \eta\} \end{aligned} \quad (26)$$

We can see that under non-ideal quantum efficiency condition, the resolution M of the PNR(M) in the DSR does not affect the error probability. Fig. 5(a) illustrates the variation of $P_{\text{err}}^{\text{DSR}}(N, \eta)$ (Eq. (26)) with respect to the average signal photon number N for $\eta = 1.0, 0.9$, and 0.8 . As shown, the three curves surpass the SQL of S-BPSK at $N = 0.30, 0.39$, and 0.56 , respectively. Moreover, as N increases, the performance advantage of $P_{\text{err}}^{\text{DSR}}(N, \eta)$ over the SQL becomes more pronounced. At $N = 1.0$, the ratios of the three curves to the SQL are -4.5 dB, -7.97 dB, -11.44 dB, respectively.

Likewise, if only consider dark counts ($\eta = 1, \nu > 0$), the optimal threshold n_{th}^* reads:

$$n_{th}^* = \min \left\{ \left\lceil \frac{|\gamma|^2}{\ln(|\gamma|^2 + \nu) - \ln \nu} \right\rceil, M \right\} = \min \left\{ \left\lceil \frac{4N(N+1)}{\ln(4N(N+1) + \nu) - \ln \nu} \right\rceil, M \right\} \quad (27)$$

As shown, under non-ideal dark count conditions, n_{th}^* is not always unity and varies with the average photon number (see Fig. 5(c)). In other words, in non-ideal dark count condition, the error probability of the DSR is correlated with the resolution of the PNR.

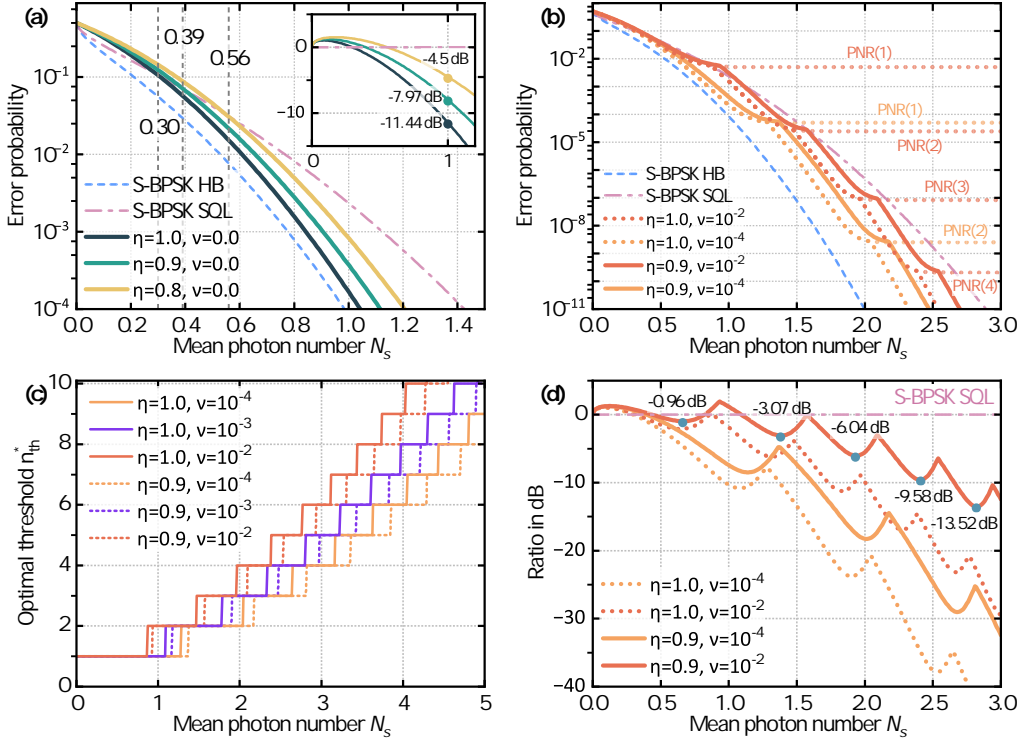


FIG. 5. Performance of the DSR with a non-ideal PNR(M) which quantum efficiency $\eta < 1$ and dark count $\nu > 0$. (a) and (b) Error probability of the DSR. (c) Optimal threshold n_{th}^* . (d) Ratio (in dB) of the benchmark P_{SQL}^{DSR} relative to P_{err} .

Fig. 5(b) shows the error probability as a function of the average signal photon number under two scenarios: considering only non-ideal dark counts, and considering both non-ideal detection efficiency and dark counts. In the presence of dark counts, the error probability exhibits an oscillatory pattern, which results from the continuous increase of the optimal threshold. This optimal threshold is limited by the resolution of the PNR detector; once it reaches the maximum resolvable photon number, the error probability no longer decreases with increasing average photon number but instead saturates. Furthermore, we observe that for curves with the same dark count rate but different detection efficiencies, the saturated error probabilities coincide. In contrast, for curves with the same detection efficiency but different dark count, a lower dark count leads to a lower saturated error probability.

We therefore conclude that the saturated error probability is determined primarily by the dark count, and its effect cannot be mitigated by increasing the signal strength. On the other hand, the performance degradation caused by non-ideal detection efficiency can be compensated by using a stronger signal. For practical PNR detectors, high detection efficiency and low dark count rate generally exhibit a trade-off relationship; improving the detection efficiency typically increases the dark count [28, 29]. Hence, in actual experiments, it can be beneficial to moderately reduce the detection efficiency in order to obtain a lower dark count, while compensating for the resultant loss in sensitivity by increasing the signal power.

In addition, a high dark count forces the optimal threshold to increase frequently until it reaches the resolution limit of the PNR detector, thereby driving the DSR scheme into saturation (see Fig. 5(c)). Consequently, a configuration with lower detection efficiency and lower dark count can alleviate the requirement for a PNR detector with very high resolution. Fig. 5(d) plots the ratio (in dB) of the error probability to the SQL of S-BPSK. It can be seen that even with both non-ideal detection efficiency and dark counts, the DSR scheme still surpasses the SQL of S-BPSK. For example, when $\eta = 0.9$ and $\nu = 10^{-2}$, the error probability of DSR with PNR(M) is lower than the SQL by -0.96dB (M=1), -3.07dB (M=2), -6.04dB (M=3), -9.58dB (M=4), and -13.52dB (M=5).

B. Phase Diffuse Noise in communication channel

Phase diffusion noise is a common communication channel noise that increases the overlap between states (S-BPSK), making them more difficult to distinguish [20, 24]. A schematic of a phase diffusion noise channel is shown in Fig. 6.

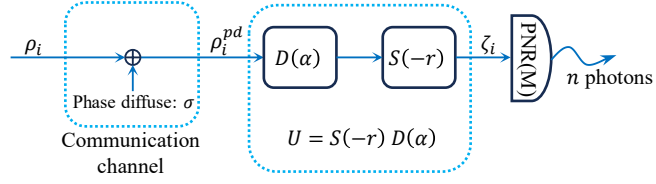


FIG. 6. Schematic diagram of phase diffusion noise channel. The signal state ρ_i (pure state) is transformed into the state ρ_i^{pd} (mixed state) in the phase diffuse communication channel.

After DSSs are contaminated by phase diffusion noise in the channel, they evolve from pure states to mixed states and can only be expressed using density operators. Let the uncontaminated DSS be denoted as $\rho_i = |\psi_i\rangle\langle\psi_i|$. The expression for the contaminated quantum state ρ_i^{pd} is then:

$$\begin{aligned}\rho_i^{pd} &= \int_{-\infty}^{+\infty} d\phi \cdot \{g_\sigma(\phi) \cdot \rho_{i,\phi}\} \\ &= \int_{-\infty}^{+\infty} d\phi \cdot \{g_\sigma(\phi) \cdot R_\phi \rho_i R_\phi^\dagger\}\end{aligned}\quad (28)$$

Here, $g_\sigma(\phi) = \frac{1}{\sqrt{2\pi\sigma^2}} \exp\left\{-\frac{\phi^2}{2\sigma^2}\right\}$ is a Gaussian function with mean 0 and standard deviation σ , which quantifies the noise strength. The rotation operator $R_\phi = e^{-j\phi a^\dagger a}$ rigidly rotates the entire Wigner function distribution of the quantum state by an angle ϕ in phase space. We denote the rotated quantum state as

$$\begin{aligned}\rho_{i,\phi} &= |\psi_{i,\phi}\rangle\langle\psi_{i,\phi}| \\ |\psi_{i,\phi}\rangle &= R_\phi |\psi_i\rangle = D((-1)^{i+1} \alpha e^{-j\phi}) S(re^{-j2\phi}) |0\rangle\end{aligned}\quad (29)$$

Thus, phase diffusion noise applies a Gaussian-distributed random phase rotation to the input signal, resulting in a completely positive map that transforms the input Gaussian state ρ_i into a non-Gaussian state ρ_i^{pd} . The phase-space evolution of quantum state ρ_i under phase diffusion noise is illustrated in Fig. 7, with signal mean photon number $N = 1.0$ and a noise strength of $\sigma = 0.5$.

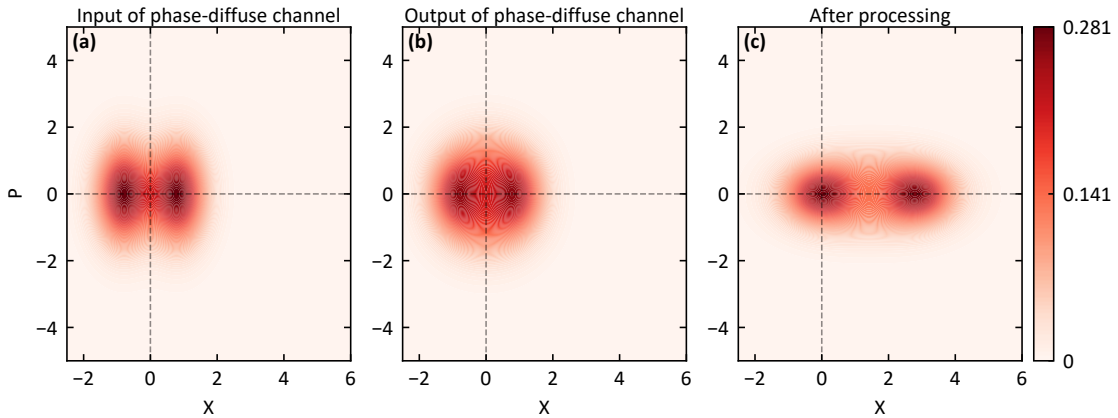


FIG. 7. Phase-space representations of S-BPSK signal (mean photon number $N = 1.0$ and phase diffusion strength $\sigma = 0.5$). (a) DSSs ρ_i without phase diffusion noise; (b) states ρ_i^{pd} with phase diffusion noise; (c) states ζ_i after DSR processing.

For the DSR receiver, since the input state ρ_i^{pd} is no longer Gaussian, the quantum state ζ_i after displacement-

squeezing processing and prior to PNR detection also ceases to be Gaussian.

$$\begin{aligned}
\zeta_i &= U \rho_i^{\text{pd}} U^\dagger \\
&= \int_{-\infty}^{+\infty} d\phi \cdot \left\{ g(\phi) \cdot U R_\phi \rho_i R_\phi^\dagger U^\dagger \right\} \\
&= \int_{-\infty}^{+\infty} d\phi \cdot \left\{ g(\phi) \cdot |\psi'_{i,\phi}\rangle \langle \psi'_{i,\phi}| \right\}
\end{aligned}$$

where,

$$\begin{aligned}
|\psi'_{0,\phi}\rangle &= U \cdot |\psi_{0,\phi}\rangle = S(-r) D(-\alpha e^{-j\phi} + \alpha) S(r e^{-j2\phi}) |0\rangle \\
|\psi'_{1,\phi}\rangle &= U \cdot |\psi_{1,\phi}\rangle = S(-r) D(+\alpha e^{-j\phi} + \alpha) S(r e^{-j2\phi}) |0\rangle
\end{aligned} \tag{30}$$

Therefore, when measuring the quantum state ζ_i with PNR(M), the probability of obtaining a detection result of n photons is:

$$\begin{aligned}
q_n^M(\zeta_i) &= \text{Tr} \{ \Pi_n \cdot \zeta_i \} \\
&= \int_{-\infty}^{+\infty} d\phi \cdot g_\sigma(\phi) \cdot \text{Tr} \{ \Pi_n \cdot |\psi'_{i,\phi}\rangle \langle \psi'_{i,\phi}| \}
\end{aligned} \tag{31}$$

By substituting into Eq. (17) and Eq. (19), we obtain the optimal threshold and the error probability of the DSR under phase diffusion noise, respectively.

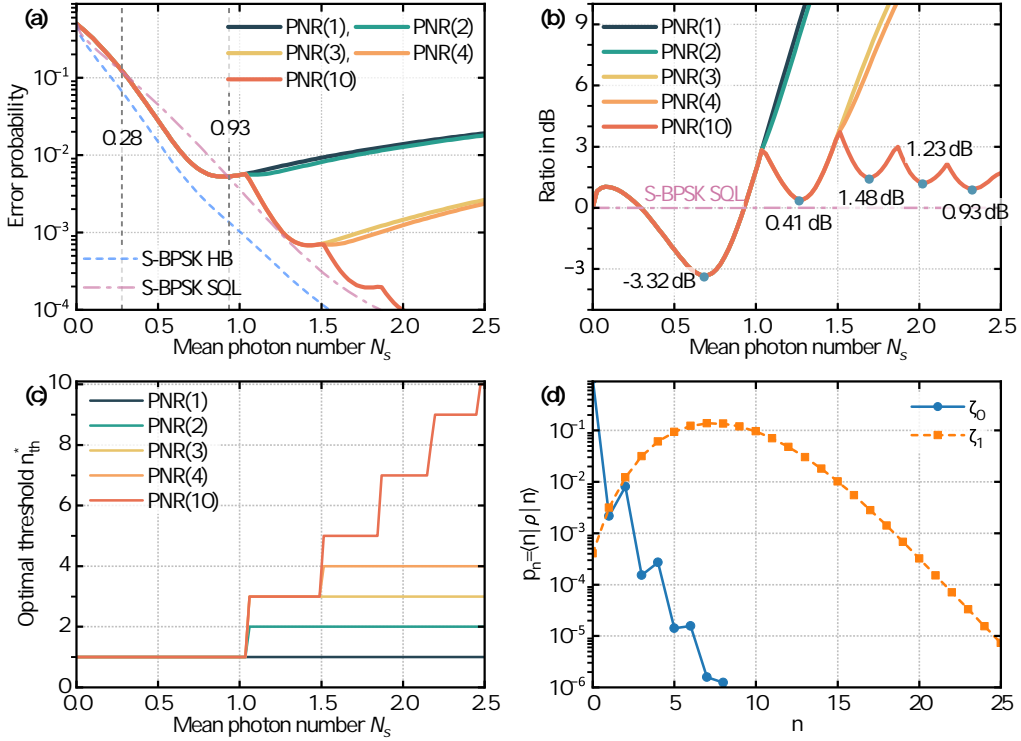


FIG. 8. Simulation results of DSR under phase diffusion noise ($\sigma = 0.1$): (a) Error probability, (b) Ratio (in dB) with a benchmark of $P_{\text{SQL}}^{\text{DSS}}$ (Eq. (B1)), (c) Optimal threshold n_{th}^* and (d) Fock-basis population of measured states $\zeta_i = U \rho_i^{\text{pd}} U^\dagger$ by PNR(M), which $N = 1.0$. *Note:* the SQL and HB of S-BPSK under phase diffusion condition is rewritten as Eq. (B1) and Eq. (B3).

Fig. 8(c) shows the variation of the optimal threshold n_{th}^* for DSR with the mean photon number under a phase diffusion of $\sigma = 0.1$. In the absence of resolution limits from the PNR detector, n_{th}^* increases in steps of 2, which differs from the behaviors previously analyzed for dark counts and thermal noise. This is attributed to the fact that,

in the presence of phase diffusion noise, DSR cannot transform ρ_0^{pd} into the vacuum state or a coherent state with a very small mean photon number (see Fig. 7(c)). After DSR processing, the Fock-basis population of the resulting state ζ_i shows a feature reminiscent of squeezed states: the populations of certain even photon numbers become higher than those of adjacent odd photon numbers, as illustrated in Fig. 8(d).

Fig. 8(c) and (b) depict the performance of DSR as a function of the mean signal photon number under a phase diffusion strength of $\sigma = 0.1$. The results show that DSR can surpass the SQL of the S-BPSK scheme within a certain photon-number range ($N \in (0.28, 0.93)$), achieving a maximum advantage of 3.32 dB beyond the SQL. However, at high photon numbers, DSR no longer exceeds the SQL. In particular, when the optimal threshold reaches the maximum resolution limit of the PNR detector, the error probability does not saturate but instead increases with the mean photon number. Furthermore, we observe that a PNR detector with a resolution of $2n$ (even) provides only marginal improvement in DSR performance compared to one with a resolution of $2n-1$; no pronounced oscillatory drop in error probability is evident. This behavior is consistent with the variation in the optimal threshold, as shown in panel (c).

C. Thermal noise in the receiver

After contamination by thermal noise, the optical states are generally mixed and should be described by density operators. Following the Glauber–Sudarshan representation, the impact of thermal background at the receiver can be modeled as a classical, Gaussian-distributed random displacement in phase space, whose statistics are independent of the input state [23, 30–32]. Accordingly, for an arbitrary input state ρ_i , the thermal-noise channel can be written as

$$\rho_i^{\text{th}} = \Phi_{n_t}(\rho_i) = \int_{\mathbb{C}} d^2\lambda f_{n_t}(\lambda) D(\lambda) \rho_i D^\dagger(\lambda), \quad (32)$$

where $D(\lambda) = \exp(\lambda a^\dagger - \lambda^* a)$ denotes the displacement operator and

$$f_{n_t}(\lambda) = \frac{1}{\pi n_t} \exp\left(-\frac{|\lambda|^2}{n_t}\right)$$

is the circularly symmetric complex Gaussian distribution. Here n_t is the mean photon number of the thermal background mode, which under thermal equilibrium is

$$n_t = \left[\exp\left(\frac{h\nu}{kT_0}\right) - 1 \right]^{-1},$$

with h the Planck constant, k the Boltzmann constant, ν the optical frequency, and T_0 the receiver temperature. In practical fiber-optic communication systems, the receiver-originated background often dominates over the channel-induced thermal noise [33].

Consistent with [30, 31], we assume that the thermal-noise contamination occurs immediately before the PNR detector, as illustrated in Fig. 9.

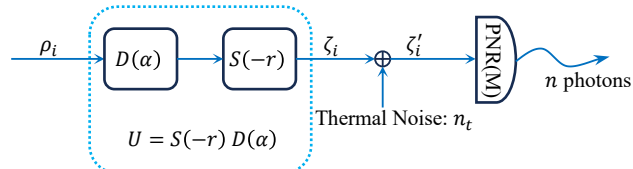


FIG. 9. Schematic of the DSR under receiver thermal noise. The processed states ζ_i impinging on the PNR(M) are contaminated by receiver thermal noise and become ζ'_i .

Remark (coherent state \Rightarrow displaced thermal state): Under the channel Φ_{n_t} in Eq. (32), a coherent-state input becomes a displaced thermal state. Specifically, using the Weyl relation $D(\lambda)D(\alpha) = e^{(\lambda\alpha^* - \lambda^*\alpha)/2}D(\lambda + \alpha)$, one verifies the displacement covariance

$$\Phi_{n_t}(D(\alpha)\rho D^\dagger(\alpha)) = D(\alpha)\Phi_{n_t}(\rho)D^\dagger(\alpha). \quad (33)$$

Moreover, by definition of Eq. (32), $\Phi_{n_t}(|0\rangle\langle 0|) = \int_{\mathbb{C}} d^2\lambda f_{n_t}(\lambda) |\lambda\rangle\langle\lambda|$ is exactly a thermal state with mean photon number n_t , denoted as $\rho_{\text{th}}(n_t)$. Therefore, for $|\alpha\rangle = D(\alpha)|0\rangle$,

$$\Phi_{n_t}(|\alpha\rangle\langle\alpha|) = \Phi_{n_t}(D(\alpha)|0\rangle\langle 0|D^\dagger(\alpha)) = D(\alpha)\rho_{\text{th}}(n_t)D^\dagger(\alpha). \quad (34)$$

Consequently, the states ζ_i measured by PNR(M), originally $|0\rangle$ and $|2\alpha e^r\rangle$, are transformed into

$$\begin{aligned} \zeta'_0 &= \Phi_{n_t}(|0\rangle\langle 0|) = \int_{\mathbb{C}} d^2\lambda f_{n_t}(\lambda) |\lambda\rangle\langle\lambda|, \\ \zeta'_1 &= \Phi_{n_t}(|2\alpha e^r\rangle\langle 2\alpha e^r|) = \int_{\mathbb{C}} d^2\lambda f_{n_t}(\lambda) |\lambda + 2\alpha e^r\rangle\langle\lambda + 2\alpha e^r|. \end{aligned} \quad (35)$$

Equivalently, by Eq. (34), one may write $\zeta'_0 = \rho_{\text{th}}(n_t)$ and $\zeta'_1 = D(2\alpha e^r)\rho_{\text{th}}(n_t)D^\dagger(2\alpha e^r)$.

Thus, under receiver thermal noise, ζ'_0 and ζ'_1 are classical mixtures of coherent states. The probability of detecting n photons with PNR(M) is

$$q_n^M(\zeta'_i) = \text{Tr}(\Pi_n \zeta'_i) = \int_{\mathbb{C}} d^2\lambda f_{n_t}(\lambda) q_n^M[\mu_i(\lambda)], \quad (36)$$

where Π_n is the POVM element corresponding to outcome n , and $\mu_0(\lambda) = |\lambda|^2$, $\mu_1(\lambda) = |\lambda + 2\alpha e^r|^2$. Substituting Eq. (36) into Eq. (17) and Eq. (19) yields the optimal threshold n_{th}^* and the error probability $P_{\text{err}}^{\text{DSR}}$ of the DSR in the presence of receiver thermal noise, respectively.

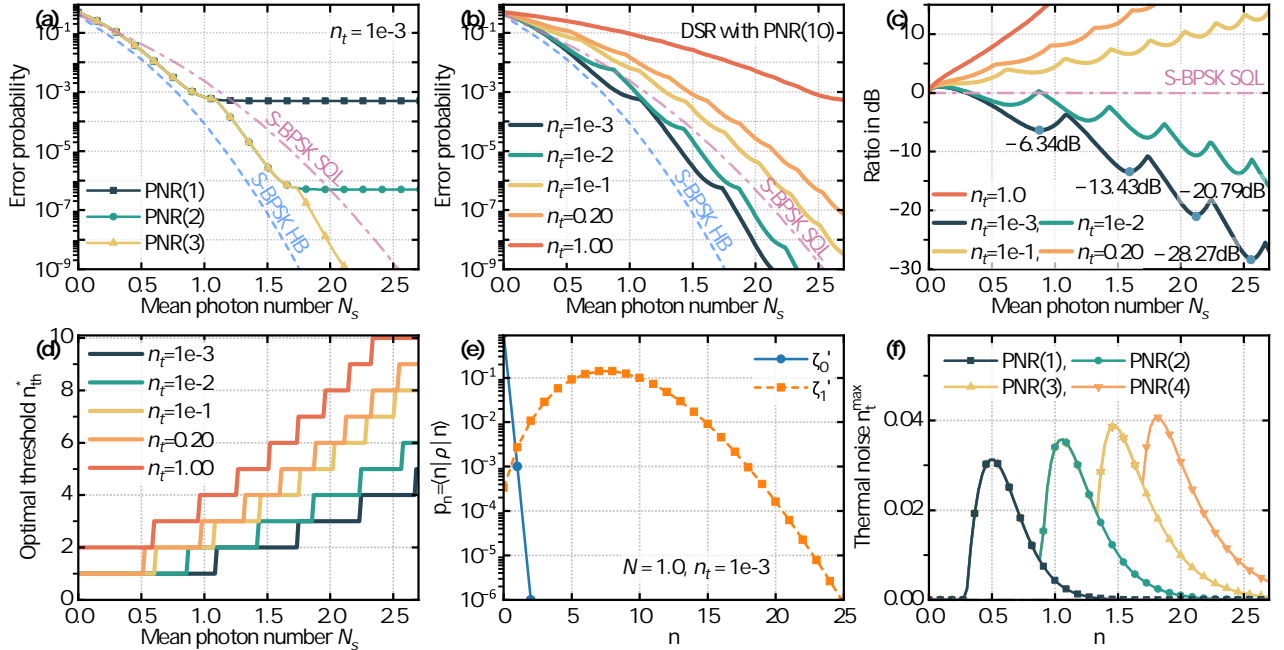


FIG. 10. Simulation results of DSR with PNR(M) under thermal noise condition: (a) Error probability ($n_t = 0.001$), (b) Error probability ($M = 10$), (c) Ratio (in dB) of the benchmark $P_{\text{err}}^{\text{DSS}}$ ($M = 10$) to the SQL of standard BPSK versus the mean signal photon number under different noise strengths. It can be observed that the DSR can still surpass the SQL at certain noise levels. For instance, when $n_t = 10^{-3}$, the error probability of the DSR with a PNR(M) detector is lower than the SQL by -6.34dB (M=1), -13.43dB (M=2), -20.79dB (M=3), and -28.27dB (M=4).

Fig. 10(a) and (b) depict the error probability of the DSR as a function of the mean signal photon number, under different PNR detector resolutions and various thermal noise strengths. The error probability curves exhibit an oscillatory pattern and decrease overall with increasing signal energy, which is a consequence of the continuous adjustment of the optimal threshold n_{th}^* (see panel (d)). This trend continues until n_{th}^* reaches the maximum resolution of the PNR detector, after which the error probability saturates and no longer varies with the mean photon number. Fig. 10(c) shows the ratio (in dB) of the DSR error probability to the SQL of standard BPSK versus the mean signal photon number under different noise strengths. It can be observed that the DSR can still surpass the SQL at certain noise levels. For instance, when $n_t = 10^{-3}$, the error probability of the DSR with a PNR(M) detector is lower than the SQL by -6.34dB (M=1), -13.43dB (M=2), -20.79dB (M=3), and -28.27dB (M=4).

Furthermore, we note that n_{th}^* increases in steps of one until it attains the maximum resolution of the PNR detector. This occurs because the Fock-basis population of the thermal-noise-perturbed state ζ'_0 still decreases monotonically with increasing photon number. This behavior differs from that under phase-diffusion noise (see Fig. 8(d)).

We then introduce the maximum tolerable thermal noise n_t^{\max} as a figure of merit, defined as the highest noise level for which $P_{\text{err}}^{\text{DSR}} \leq P_{\text{SQL}}^{\text{DSS}}$ at a given signal energy N . This quantity is shown in Fig. 10(e). Thus, the DSR outperforms the SQL when $n_t < n_t^{\max}$, corresponding to the region below the n_t^{\max} curve. The plot displays M distinct peaks, after which it decays toward zero.

V. CONCLUSION

We presented a displacement-squeeze receiver for S-BPSK discrimination based on Gaussian preprocessing and PNR/MAP thresholding. In the ideal, equal-prior case, $n_{\text{th}}^* = 1$ and $P_{\text{err}}^{\text{DSR}} = \frac{1}{2} \exp[-4N(N+1)]$, independent of the PNR number resolution. The resulting performance is provably within a constant factor of the S-BPSK Helstrom bound for all N , $P_{\text{err}}^{\text{DSR}} \in [P_{\text{HB}}^{\text{DSS}}, 2P_{\text{HB}}^{\text{DSS}}]$, while surpassing the S-BPSK SQL at $N \approx 0.3$ and the C-BPSK Helstrom bound at $N \approx 0.4$ (sub-1% errors near $N \approx 0.6$). Under nonideal operation, we modeled detector inefficiency and dark counts, channel phase diffusion, and receiver thermal noise, and found that adaptive MAP thresholds maintain an advantage over the SQL within practical ranges (e.g., under $\sigma = 0.1$, DSR exceeds the S-BPSK SQL for $N \in (0.28, 0.93)$).

Future work includes extending the architecture to multi-ary constellations (e.g., QPSK and 16QAM) and validating performance in hardware under dynamic channel conditions.

Appendix A: The Wigner Function of Displaced Squeezed Vacuum States

The Displaced Squeezed States (DSSs) discussed in this paper belong to single-mode Gaussian states, whose Wigner function is a bivariate Gaussian distribution fully characterized by two parameters: the displacement vector \vec{d} and the covariance matrix \mathbf{V} . Given a DSS denoted as $|\psi\rangle$, its quantum mechanical expression is

$$|\psi\rangle = |\alpha, r\rangle = D(\alpha)S(r)|0\rangle, \quad \alpha, r \in \mathbb{R}_+. \quad (\text{A1})$$

The first parameter, the displacement vector \vec{d} , is a two-dimensional vector representing the translation in phase space relative to the origin. Its components correspond to the expectation values of the quadrature operators \hat{X}, \hat{P} :

$$\vec{d} = \begin{pmatrix} d_x \\ d_p \end{pmatrix} = \begin{pmatrix} \langle \hat{X} \rangle \\ \langle \hat{P} \rangle \end{pmatrix}. \quad (\text{A2})$$

For $|\psi\rangle$, $d_x = \sqrt{2}\text{Re}(\alpha) = \sqrt{2}\alpha$ and $d_p = \sqrt{2}\text{Im}(\alpha) = 0$. The second parameter, the covariance matrix \mathbf{V} , is a 2×2 real symmetric positive-definite matrix describing the “shape” and “size” of the quantum state in phase space. Its elements are variances and covariances:

$$\begin{aligned} \mathbf{V} &= \begin{bmatrix} V_{xx} & V_{xp} \\ V_{px} & V_{pp} \end{bmatrix} \\ &= \begin{bmatrix} \langle (\Delta \hat{X})^2 \rangle & \frac{1}{2} \langle \{\Delta \hat{X}, \Delta \hat{P}\} \rangle \\ \frac{1}{2} \langle \{\Delta \hat{X}, \Delta \hat{P}\} \rangle & \langle (\Delta \hat{P})^2 \rangle \end{bmatrix}, \end{aligned} \quad (\text{A3})$$

where $\Delta \hat{O} = \hat{O} - \langle \hat{O} \rangle$, and the anticommutator is defined as $\{\hat{A}, \hat{B}\} = \hat{A}\hat{B} + \hat{B}\hat{A}$. For $|\psi\rangle$, the covariance matrix is

$$\mathbf{V} = \begin{bmatrix} \frac{1}{2}e^{-2r} & 0 \\ 0 & \frac{1}{2}e^{2r} \end{bmatrix}, \quad (\text{A4})$$

indicating that in phase space, the state is an ellipse (coherent states and vacuum states appear as circles), with fluctuations squeezed along the X -direction and expanded along the P -direction, while the overall phase-space area remains unchanged ($\det \mathbf{V} = \frac{1}{2}e^{-2r} \cdot \frac{1}{2}e^{2r} = \frac{1}{4}$).

Substituting \vec{d} and \mathbf{V} into the general formula yields the Wigner function for $|\psi\rangle$:

$$\begin{aligned} W(\vec{r}|\psi) &= \frac{1}{2\pi\sqrt{\det \mathbf{V}}} \exp\left\{-\frac{1}{2}(\vec{r}-\vec{d})^T \mathbf{V}^{-1}(\vec{r}-\vec{d})\right\} \\ &\rightarrow W(x, p|\psi) = \frac{1}{\pi} \exp\left\{-e^{2r}(x - \sqrt{2}\alpha)^2 - e^{-2r}p^2\right\}, \end{aligned} \quad (\text{A5})$$

where $\vec{r} = \begin{pmatrix} x \\ p \end{pmatrix}$ is a point in phase space, and $\det \mathbf{V}$ denotes the determinant of \mathbf{V} .

Appendix B: The Helstrom bound and SQL of S-BPSK under phase diffusion condition

Phase diffusion noise is a communication channel noise, therefore theoretically both the Helstrom bound and the SQL for S-BPSK ρ_i^{pd} (Eq. (28)) are affected. Specifically, the SQL expression in Eq. (4) should be rewritten as:

$$\begin{aligned} P_{\text{SQL}}^{\text{DSS}}(N, \sigma) &= \int_0^{+\infty} dx \cdot P(x|\rho_i^{\text{pd}}) \\ &= \int_0^{+\infty} dx \int_{\mathbf{R}} d\phi \cdot g_{\sigma}(\phi) \cdot P(x|\rho_{i,\phi}) \\ &= \int_0^{+\infty} dx \int_{\mathbf{R}} d\phi \cdot g_{\sigma}(\phi) \int_{\mathbf{R}} dp \cdot W(x, p|\rho_{i,\phi}) \\ &= \int_{\mathbf{R}} d\phi \cdot g_{\sigma}(\phi) \cdot P_{\text{SQL}}^{\text{DSS}}(\phi) \end{aligned} \quad (\text{B1})$$

Here,

$$P_{\text{SQL}}^{\text{DSS}}(\phi) = \int_0^{+\infty} dx \cdot P(x|\rho_{i,\phi}) = \int_0^{+\infty} dx \int_{\mathbf{R}} dp \cdot W(x, p|\rho_{i,\phi}) \quad (\text{B2})$$

represents the SQL for the binary quantum states $\{\rho_{0,\phi}, \rho_{1,\phi}\}$ (see Eq. (29)). $P(x|\rho_{i,\phi})$ is the homodyne probability of obtaining outcome x given the state $\rho_{i,\phi}$. Note: The rotation operator R_{ϕ} is a Gaussian operator, thus $\rho_{i,\phi}$ remains a Gaussian state. Its Wigner function can be computed using the method described in Appendix A.

For the Helstrom limit of two states ρ_i^{pd} , Eq. (2) (applicable only to pure states) is no longer suitable and should be replaced with its equivalent form:

$$P_{\text{HB}}^{\text{DSS}}(N, \sigma) = \frac{1}{2} \left(1 - \left\| P_0 \rho_0^{\text{pd}} - P_1 \rho_1^{\text{pd}} \right\|_1 \right) \quad (\text{B3})$$

where $\|A\|_1 = \text{Tr}\{A^{\dagger}A\}$ denotes the trace norm, and P_0, P_1 denote prior probabilities. This expression applies to the calculation of the Helstrom bound for binary states, whether pure or mixed.

ACKNOWLEDGMENTS

This work was supported by Independent Innovation Science Fund Program of National University of Defense Technology, China (Grant No. 22-ZZCX-036), Key research&development program of Guangxi (Grant No. GuiKeAB23075155), the National Science Foundation for Young Scientists of China (Grant No. 12204539), and the Key Research & Development Program of Guangxi (Grant No. AB23075112).

DATA AVAILABILITY

The data that support the findings of this article are not publicly available. The data are available from the authors upon reasonable request.

[1] R. S. Kennedy, A near-optimum receiver for the binary coherent state quantum channel, Research Laboratory of Electronics, MIT, Quarterly Progress Report **108**, 219 (1973).

- [2] M. Takeoka and M. Sasaki, Discrimination of the binary coherent signal: Gaussian-operation limit and simple non-gaussian near-optimal receivers, *Phys. Rev. A* **78**, 022320 (2008).
- [3] V. A. Vilnrotter, Quantum receiver for distinguishing between binary coherent-state signals with partitioned-interval detection and constant-intensity local lasers, *NASA IPN Progress Report* **42** (2012).
- [4] S. Izumi, M. Takeoka, M. Fujiwara, N. D. Pozza, and M. Sasaki, Quantum displacement receiver for m-ary phase-shift-keyed coherent states, *Physical Review A* **86**, 042328 (2012).
- [5] T. Chen, K. Li, Y. Zuo, and B. Zhu, *Qam adaptive measurements feedback quantum receiver performance* (2015), [arXiv:1504.02859 \[quant-ph\]](https://arxiv.org/abs/1504.02859).
- [6] R. Nair, S. Guha, and S.-H. Tan, A realizable receiver for discriminating arbitrary coherent states near the quantum limit, in *2013 IEEE International Symposium on Information Theory* (2013) pp. 729–733.
- [7] Y. Zuo, T. Chen, and B. Zhu, Conditional pulse nulling receiver for multi-pulse PPM and binary quantum coding signals, in *Fourth International Conference on Wireless and Optical Communications*, Vol. 9902, edited by M. Ma, International Society for Optics and Photonics (SPIE, 2016) p. 99020V.
- [8] C. R. Müller, M. A. Usuga, C. Wittmann, M. Takeoka, C. Marquardt, U. L. Andersen, and G. Leuchs, Quadrature phase shift keying coherent state discrimination via a hybrid receiver, *New Journal of Physics* **14**, 083009 (2012).
- [9] A. Allevi, M. Bina, S. Olivares, and M. Bondani, Hybrid homodyne-like detection scheme with photon-number-resolving detectors, in *2017 Progress In Electromagnetics Research Symposium - Spring (PIERS)* (2017) pp. 2874–2878.
- [10] M. N. Notarnicola, M. G. A. Paris, and S. Olivares, Hybrid near-optimum binary receiver with realistic photon-number-resolving detectors, *Journal of the Optical Society of America B* **40**, 705 (2023).
- [11] Y. Zuo, K. Li, and B. Zhu, 16-qam quantum receiver with hybrid structure outperforming the standard quantum limit, *MATEC Web of Conferences* **61**, 06008 (2016).
- [12] V. Giovannetti, S. Guha, S. Lloyd, L. Maccone, J. H. Shapiro, and H. P. Yuen, Classical capacity of the lossy bosonic channel: The exact solution, *Phys. Rev. Lett.* **92**, 027902 (2004).
- [13] M. M. Wolf, D. Pérez-García, and G. Giedke, Quantum capacities of bosonic channels, *Phys. Rev. Lett.* **98**, 130501 (2007).
- [14] L. Lami, K. K. Sabapathy, and A. Winter, All phase-space linear bosonic channels are approximately gaussian dilatable, *NEW JOURNAL OF PHYSICS* **20**, 10.1088/1367-2630/aae738 (2018).
- [15] C. W. Helstrom, Quantum detection and estimation theory, *Journal of Statistical Physics* **1**, 231 (1969).
- [16] A. S. Holevo, Bounds for the quantity of information transmitted by a quantum communication channel, *Problemy Peredachi Informatsii* **9**, 3 (1973).
- [17] M. G. A. Paris, Nearly ideal binary communication in squeezed channels, *Phys. Rev. A* **64**, 014304 (2001).
- [18] S. Izumi, M. Takeoka, K. Ema, and M. Sasaki, Quantum receivers with squeezing and photon-number-resolving detectors for m -ary coherent state discrimination, *Phys. Rev. A* **87**, 042328 (2013).
- [19] R. Schnabel, Squeezed states of light and their applications in laser interferometers, *Physics Reports* **684**, 1 (2017), squeezed states of light and their applications in laser interferometers.
- [20] G. Chesi, S. Olivares, and M. G. A. Paris, Squeezing-enhanced phase-shift-keyed binary communication in noisy channels, *Phys. Rev. A* **97**, 032315 (2018).
- [21] I. A. Burenkov, M. V. Jabir, and S. V. Polyakov, Practical quantum-enhanced receivers for classical communication, *AVS Quantum Science* **3**, 025301 (2021), https://pubs.aip.org/avs/aqs/article-pdf/doi/10.1116/5.0036959/19739052/025301_1_online.pdf.
- [22] A. Walsh, L. Conlon, B. Shajilal, O. Erkilic, J. Janousek, S. Assad, J. Zhao, and P. K. Lam, *All-gaussian state discrimination beyond the coherent helstrom bound* (2025), [arXiv:2510.20096 \[quant-ph\]](https://arxiv.org/abs/2510.20096).
- [23] R. Yuan, M. Zhao, S. Han, and J. Cheng, Kennedy receiver using threshold detection and optimized displacement under thermal noise, *IEEE Communications Letters* **24**, 1313 (2020).
- [24] M. N. Notarnicola and S. Olivares, A robust hybrid receiver for binary phase-shift keying discrimination in the presence of phase noise, *International Journal of Quantum Information* **22**, 2450008 (2024), <https://doi.org/10.1142/S0219749924500084>.
- [25] G. Humer, M. Peev, C. Schaeff, S. Ramelow, M. Stipčević, and R. Ursin, A simple and robust method for estimating afterpulsing in single photon detectors, *Journal of Lightwave Technology* **33**, 3098 (2015).
- [26] C. Ding, X. Zhang, J. Xiong, Y. Xiao, T. Zhang, J. Huang, H. Xu, X. Liu, L. You, Z. Wang, and H. Li, Photon-number-resolving single-photon detector with a system detection efficiency of 98% and photon-number resolution of 32, *ACS Photonics* **12**, 4924 (2025), <https://doi.org/10.1021/acsphotonics.5c00508>.
- [27] S. M. Barnett, L. S. Phillips, and D. T. Pegg, Imperfect photodetection as projection onto mixed states, *Optics Communications* **158**, 45 (1998).
- [28] L. Zhang, L. Kang, J. Chen, Y. Zhong, Q. Zhao, T. Jia, C. Cao, B. Jin, W. Xu, G. Sun, and P. Wu, Ultra-low dark count rate and high system efficiency single-photon detectors with 50 nm-wide superconducting wires, *Applied Physics B-Lasers and Optics* **102**, 867 (2011).
- [29] C. M. Natarajan, M. G. Tanner, and R. H. Hadfield, Superconducting nanowire single-photon detectors: physics and applications, *Superconductor Science and Technology* **25**, 063001 (2012).
- [30] M. Zhao, R. Yuan, J. Cheng, and S. Han, Security of binary modulated continuous variable quantum key distribution using optimally displaced threshold detection, *IEEE Communications Letters* **25**, 1089 (2021).
- [31] R. Yuan, M. Zhao, S. Han, and J. Cheng, Optimally displaced threshold detection for discriminating binary coherent states using imperfect devices, *IEEE Transactions on Communications* **69**, 2546 (2021).
- [32] G. Cariolaro and G. Pierobon, Performance of quantum data transmission systems in the presence of thermal noise, *IEEE Transactions on Communications* **58**, 623 (2010).

[33] M. Heid and N. Lütkenhaus, Efficiency of coherent-state quantum cryptography in the presence of loss: Influence of realistic error correction, *Phys. Rev. A* **73**, 052316 (2006).